Fast Lead-Free Humidity Sensor Based on Hybrid Halide Perovskite

crystals

MDPI

Article

Fast Lead-Free Humidity Sensor Based on Hybrid Halide Perovskite

Veljko Djokić [1,2], Pavao Andričević [1,3], Márton Kollár [1], Anastasiia Ciers [1,4], Alla Arakcheeva [1], Milica Vasiljević [5], Dragan Damjanović [5], László Forró [1,6], Endre Horváth [1] and Trpimir Ivšić [1,7,*]

1 Laboratory of Physics of Complex Matter, École Polytechnique Fédérale de Lausanne (EPFL), 1015 Lausanne, Switzerland; vdjokic@tmf.bg.ac.rs (V.D.); proan@dtu.dk (P.A.); kollar7@gmail.com (M.K.); anastasiia.ciers@chalmers.se (A.C.); allaarakcheeva@gmail.com (A.A.); lforro@nd.edu (L.F.); endre.horvath@epfl.ch (E.H.)
2 Faculty of Technology and Metallurgy, University of Belgrade, 11000 Belgrade, Serbia
3 Department of Physics, Technical University of Denmark, DTU Risø Campus, 4000 Copenhagen, Denmark
4 Department of Microtechnology and Nanoscience, Chalmers University of Technology, 41296 Gothenburg, Sweden
5 Group for Ferroelectrics and Functional Oxides, École Polytechnique Fédérale de Lausanne (EPFL), 1015 Lausanne, Switzerland; mvasiljevic1011@gmail.com (M.V.); dragan.damjanovic@epfl.ch (D.D.)
6 Stavropoulos Center for Complex Quantum Matter, University of Notre Dame, Notre Dame, IN 46556, USA
7 Institute of Solid-State Physics, TU Wien, 1040 Wien, Austria
* Correspondence: trpimir.ivsic@tuwien.ac.at

Abstract: An environmentally friendly analog of the prominent methylammonium lead halide perovskite, methylammonium bismuth bromide ($MA_3Bi_2Br_9$), was prepared and investigated in the form of powder, single crystals and nanowires. Complete characterization via synchrotron X-ray diffraction data showed that the bulk crystal does not incorporate water into the structure. At the same time, water is absorbed on the surface of the crystal, and this modification leads to the changes in the resistivity of the material, thus making $MA_3Bi_2Br_9$ an excellent candidate for use as a humidity sensor. The novel sensor was prepared from powder-pressed pellets with attached carbon electrodes and was characterized by being able to detect relative humidity over the full range (0.7–96% RH) at ambient temperature. Compared to commercial and literature values, the response and recovery times are very fast (down to 1.5 s/1.5 s).

Keywords: lead-free; perovskite; environmentally friendly; humidity sensor; fast response

Citation: Djokić, V.; Andričević, P.; Kollár, M.; Ciers, A.; Arakcheeva, A.; Vasiljević, M.; Damjanović, D.; Forró, L.; Horváth, E.; Ivšić, T. Fast Lead-Free Humidity Sensor Based on Hybrid Halide Perovskite. *Crystals* **2022**, *12*, 547. https://doi.org/10.3390/cryst12040547

Academic Editor: Saripally Sudhaker Reddy

Received: 20 March 2022
Accepted: 6 April 2022
Published: 14 April 2022

1. Introduction

Lead halide perovskites have recently gained much attention, both from industry and scientific communities, due to their high potential for inclusion in electronic devices [1,2]. An example of such outstanding performance is that lead halides with methylammonium (MA) cation show excellent photoelectrical properties, which means they are a promising candidate for the massive production of next-generation solar cells [3,4]. In addition, lead perovskites show potential for application, among others, as photodetectors [5,6], LEDs [7–9], lasers, memristors [10], thermoelectrics [11] and in magnetooptical data storage [12]. On the other hand, a major drawback of this class of compounds is the toxicity of lead, which could have a high environmental impact once they start to be used on a global scale [13,14]. This has incited extensive research into related compounds in which lead would be replaced with a less toxic element. Here, bismuth compounds have emerged as promising candidates, both due to the abundance of bismuth in nature and their negligible biological effects, such that they are safely used in medications [15,16].

Several bismuth derivatives of halide perovskites were reported, and it was shown that they experience a significant shift in structure upon the change of the anion from chloride to iodide [17]. Bismuth bromide perovskites were first studied by Jakubas more than thirty years ago, when two stable derivatives were found: $MA_3Bi_2Br_9$ [18] and $MA_5Bi_6Br_{11}$ [19,20].

The former derivative shows interesting phase transitions, with the lowest temperature phase behaving as an improper ferroelectric [21,22] that was further probed by dielectric and pyroelectric measurements [23]. Moreover, the latter derivative was recently restudied due to its ferroelectric properties [24].

Quite recently, bismuth methylammonium halide perovskites were also revisited due to their potential interest for inclusion into solar cells. Iodide [17,25] and chloride [26] derivatives were studied as potential photo-active components, albeit with low power conversion efficiency. In contrast, the bromide derivative $MA_3Bi_2Br_9$ was omitted from these works and, to the best of our knowledge, its implementation into any electrical device has not yet been attempted. In addition, most of the bismuth bromide structure refinement have not determined theposition of the MA cation, but rather only suggested it by analogy to $Cs_3Bi_2Br_9$. Therefore, here, we newly studied $MA_3Bi_2Br_9$ with synchrotron XRD data and electrical measurement and further demonstrated that it is a potent humidity detector.

Measuring the relative humidity (RH) is of great importance in agriculture, climatology and automated industrial processes [27]. More recently, the application of humidity sensing expanded to healthcare as an easy way to determine respiration [28,29] as well as in the area of wearable textiles production [30] and artificial skin to monitor all the vital signs of a person [31].

Several humidity sensing devices are based on measuring the change in various optical properties of a material in contact with humidity, ranging from absorbance [32,33] fluorescence [34] and reflection [35] to wavelength shift [36] and still others. While many compounds are found to exhibit some kind of optical response when exposed to humidity, from the practical point of view, the drawback would be a requirement for precise optical sensing devices, which may deter them from utilization in everyday use.

More conveniently, changes in the electrical response of a material are measured; for example, a variation in capacitance or resistance in dependence on relative humidity. For capacitive sensors, a dielectric material is used, the capacitance of which changes upon exposure to humidity, which is measured by alternating the current at the radio frequency range. Some recent examples of studied materials include cadmium selenide quantum dots [37], graphene oxide [38] and nanodiamonds [39].

Finally, the simplest and the most common humidity sensors are of the resistive type, which exhibit variations in electrical resistance upon the adsorption of water to the surface of the material, with many representative examples known [27]. This design of the device through its simplicity allows for an easy integration with the other electronic circuits at a low cost, and also presents the first choice when testing a new material.

Following the exceptional performance of perovskite materials in other electronic devices, an attempt was made to utilize lead perovskites for humidity sensors [40], with limited success, however, since the inclusion of water into a crystal structure already occurs at 55% RH, followed by the degradation of the sensing material. In another attempt, a mixed chloride/iodide derivative was stable up to 90% RH, however, with a slow response time of 24 s [41]. In addition, most recently, a humidity sensor based on $Cs_2BiAgBr_6$ perovskite was reported [42], showing a very good performance and response time of 1.78 s.

In summary, the characteristics that define good humidity sensors are: sensibility over a wide detection range, fast response and recovery times and long-term stability. While some types of material allow for highly precise measurements, their operation is limited to a small range of relative humidity. Others are sensitive over a wider range of RH, but their response and recovery times are slow. In contrast, the new $MA_3Bi_2Br_9$-based sensors presented here show high sensibility over a broad range of RH combined with fast response and recovery times (down to 1.5 s/1.5 s).

2. Experimental Section

2.1. Synthesis

All reagents were obtained from commercial suppliers. The $MA_3Bi_2Br_9$ starting material was prepared by analogy to the lead halide perovskite already prepared in our group [43]. The flask containing $Bi(NO_3)_3 \times 5H_2O$ (4.85 g) and concentrated HBr (10 mL) was placed in an ice bath. Methylamine solution (1.3 mL) was added dropwise over 1 h. The reaction started at ~40 °C but was highly exothermic, creating brown NO_2 gas. The reaction was stirred until the formation of nitrous gas bubbles stopped, usually for more than 24 h. The mixture was put in the refrigerator at 4 °C. The shiny, yellow, plate-like crystals of $(CH_3NH_3)_3Bi_2Br_9$ were harvested after 24 h. It was found that the same product may be prepared more conveniently using acetate as a starting compound instead of nitrate.

Three types of $MA_3Bi_2Br_9$ were prepared via solution growth: powder (flakes), single crystals and nanowires (Figure 1). Crystals of $MA_3Bi_2Br_9$ were prepared directly from the reaction solution. The small, shiny, yellow flakes were harvested after slowly cooling down the reaction mixture over 24 h. The preparation of larger single crystals was performed under similar conditions over a longer time, and by making a temperature gradient in the vessel. Thus, one week after, macroscopic crystals were formed on the hot side (40 °C) of the crystallization dish.

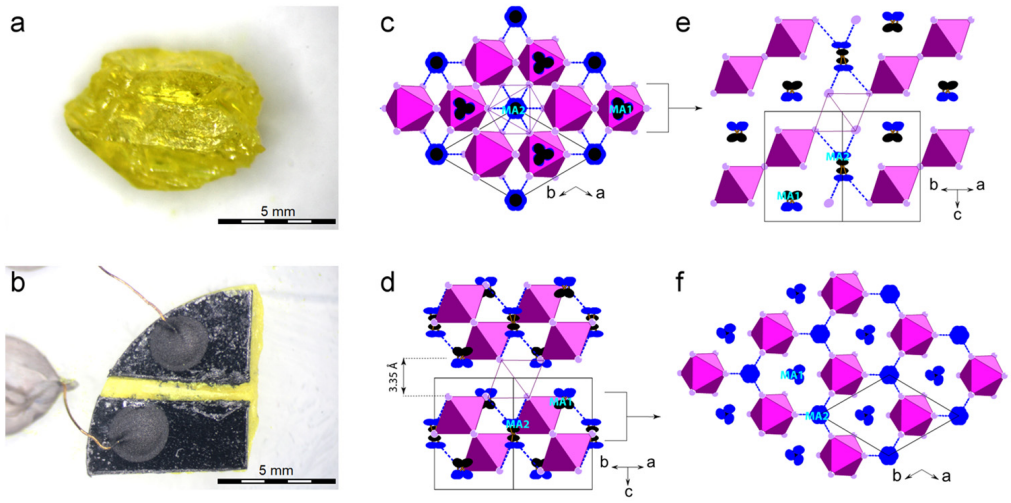

Figure 1. $MA_3Bi_2Br_9$: (**a**) single crystal, (**b**) powder pressed pellet with carbon paste and contacts attached to it, (**c**,**d**) the structure projection along the *c*-axis and the (110)-direction, respectively, (**e**) representative section of the structure parallel to the *c*-axis, (**f**) structure of one layer normal to the *c*-axis. Blue dashed lines indicate the donor–acceptor hydrogen bonds of 3.08 Å. Violet lines show the empty Br_6-octahedron.

Nanowires were prepared via the complete dissolution of $MA_3Bi_2Br_9$ flakes in DMSO and recrystallization on a substrate via the evaporation of solvent at room temperature. Solvent evaporation at temperatures higher than 80 °C leads to the formation of BiOBr as an undesired side product.

2.2. X-ray Diffraction Experiments

The synchrotron radiation single-crystal X-ray diffraction experiments were carried out with wavelength λ = 0.7129 Å at 293 K for single crystals and with λ = 0.64109 Å at 276 K for powder samples. The PILATUS@SNBL detector at the Swiss-Norwegian Beam Lines, European Synchrotron Radiation Facility [44] was used for the data detection. The powder diffraction data were processed with BUBBLE software [44]. CrysAlisPro program package was used for the single-crystal experimental data processing [45]. Structural calculations were made with JANA2006 software [46]. The main details of the experiment and crystallographic characteristics of $MA_3Bi_2Br_9$ are given in Table S1.

The powder X-ray diffractograms were taken on an Empyrean system (Theta-Theta, 240 mm) equipped with a PIXcel-1D detector, and Bragg-Brentano beam optics.

Structure solution: The structure was solved using the Superflip program [47]. The arrangement of the $BiBr_6$-octahedra was found in the space group P-3m1. N and C atoms of two MA cations were found from the difference in electron density calculated after the localization of Bi and Br atoms. CCDC number 1935075 contains the supplementary crystallographic data for this paper. These data can be obtained free of charge from The Cambridge Crystallographic Data Centre via www.ccdc.cam.ac.uk/data_request/cif, accessed on 20 March 2022.

2.3. Humidity Control

The humidity was controlled using a homemade setup (Figure 2a). A stream of synthetic air (a mixture of N_2 and O_2 at a volume ratio 78/22) with a nominal water content <3 ppm was split into two parts; one part was bubbled through the saturated water solution of $CuSO_4 \times 5H_2O$ to achieve RH ~100%. The stream of wet air was then reunited with the remaining dry air stream and guided into the sealed desiccator equipped with an exhaust pipe and electrical wires. After carefully adjusting the flow, it was possible to control the humidity in the desiccator by using the set of valves and achieve the reliable RH range from 0.7 to 95.8% measured using a commercial humidity/temperature sensor Sensirion SHT 31. Temperature was modified by putting the device on the heating plate and measured using the same (commercial) sensor. The $MA_3Bi_2Br_9$ was connected by wires and put in the desiccator next to the commercial humidity sensor.

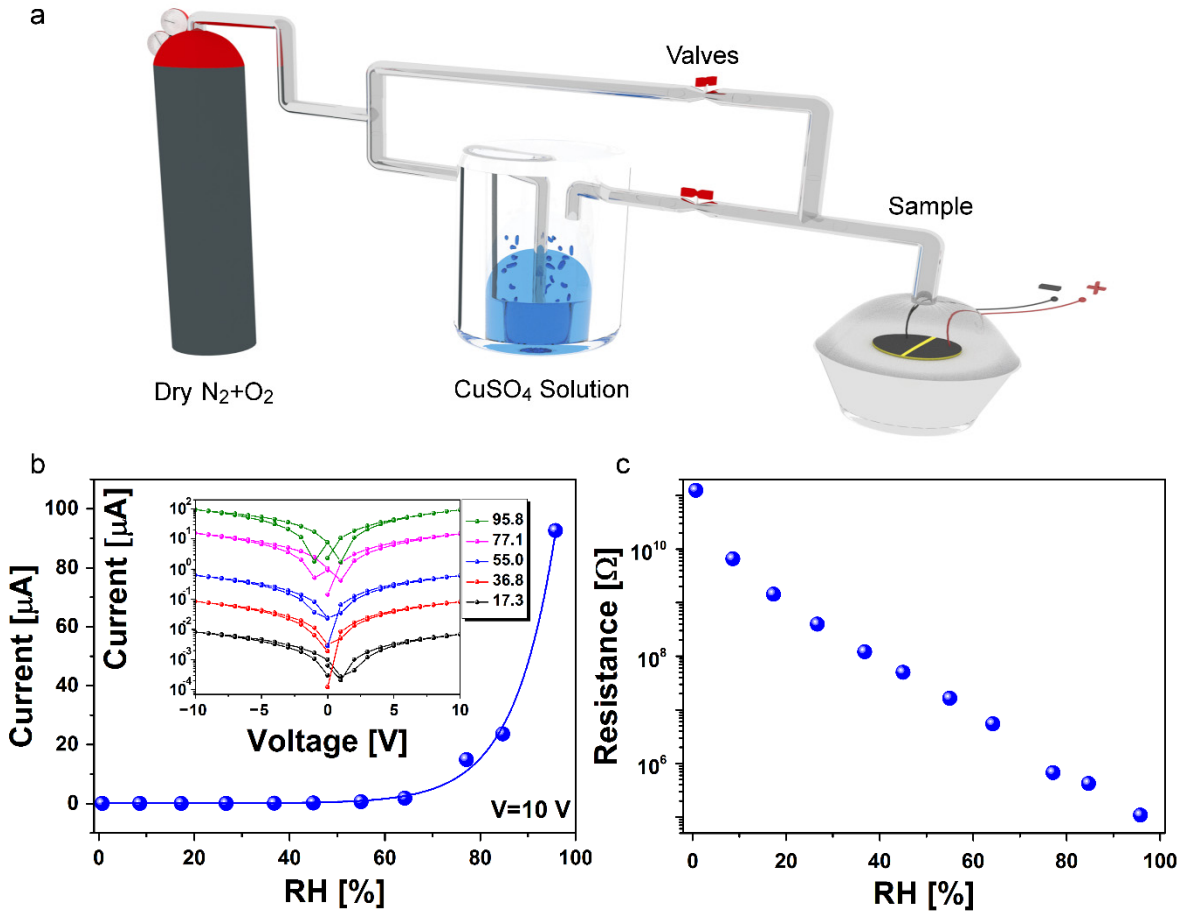

Figure 2. (**a**) Scheme of the experimental setup used for measurements. (**b**) Dependence of current at 10 V on RH at ambient temperature. The inset figure shows typical I–V curves from which the current at 10 V was extracted. (**c**) Linear dependence of the resistance of $MA_3Bi_2Br_9$ on RH.

Selected measurements were repeated in glovebox equipped with an ETS microprocessor humidification/dehumidification system model 5100, which allowed for the most precise control of the humidity.

2.4. Electrical Measurements

The properties of the powder were measured by pressing it into cylindrical pellets, together with the graphite paper as an electrical contact. When two carbon papers were pressed from each side of the pellet, a high charging effect was observed, tampering the measurements. Therefore, graphite paper was only used on one side of the pellet, with a small stripe about ~1 mm in width removed from the middle of the carbon layer. Golden wires were attached to the graphite paper using carbon paste and connected to a Keithley 2400 multimeter, as seen in Figure 1b. Experiments were performed at ambient conditions, except when noted otherwise.

AC impedance measurements were carried out on a sample with a slit electrode using an Agilent 4294A Precision Impedance Analyzer. The impedance was measured in the frequency range from 100 Hz to 2 MHz and the driving voltage was 0.5 Vrms. The sample was placed in a desiccator together with a commercial humidity meter. The humidity was controlled by placing various amounts of silica gel desiccant and water into the desiccator in a proximity of the sample and the humidity sensor. It was possible to change the relative humidity of the air in the desiccator from 8% to 90%. The humidity was changed from the lowest to the highest value.

3. Results and Discussion

3.1. Crystal Structure

The main results of the experiment, crystallographic characteristics and quality of the structure refinement of are given in Table S1. It was confirmed that $MA_3Bi_2Br_9$ belongs to the $A_3B_2X_9$ family of two-dimensional perovskites with the $Cs_3Sb_2I_9$ structure type [48], which is characterized by the space group *P*-3*m*1. MA cation plays a role of a big-size cation A and X = Br. The arrangement of the $BiBr_6$-octahedra differs from the perovskite by missing every third layer of the octahedra along the 3-fold axis (Figure 1c–f). The positions of N and C atoms of two MA cations were found from the difference in electron density calculated after the localization of Bi and Br atoms. Each N and C atom is statistically distributed in a site with higher multiplicity than one, so that the corresponding sites are partially occupied (Table S1). Hence, similar to $MAPbI_3$ [49], MA cations are partially disordered (Figure 1). The essential disorder of N and C does not allow the localization of the hydrogen positions.

3.2. Electrophysical and Sensor Properties

The photoelectrical properties of $MA_3Bi_2Br_9$ were, unfortunately, found to be poor; however, strong variations in the electrical resistance of the material was seen in the dependence of humidity, suggesting that the $MA_3Bi_2Br_9$ could be used to build an RH sensor. To thoroughly investigate this behavior of the material and potential application as a humidity sensor, three forms of $MA_3Bi_2Br_9$ were prepared and tested measuring resistivity: powder, single crystals and nanowires. The responses of the sensor at several RH are shown in the inset in Figure 2b as a set of I–V (current–voltage) curves in region −10 V to +10 V, from which the values of direct current were extracted.

It was observed that using a direct current, the sensor was operable at the full measuring range (0.7–95.8% RH); the rise in RH from 0.7% to 95.8% was followed by the rise in the measured current at 10 V from ~10^{-4} to ~10^{2} μA. The current exponentially increased with higher relative humidity (Figure 2b), whereas slight deviations were attributed to the difficulties controlling the RH at higher values. In other words, a linear trend was observed in the logarithmic scale as resistivity rose from ~10^{-5} to ~10^{1} μΩ when RH changed from 0.7% to 95.8% RH (Figure 2c).The sensitivity, which is defined as $S = |R_x - R_0|/R_0$

(where R_x and R_0 are resistance at higher and lower RH, respectively) [42] was in this case 9.5×10^3, which is sufficiently high for application in the device.

The material was also tested using alternating current (AC). The complex impedance $Z = R + iX = R - i/\omega C$ plots (plots of the imaginary ($1/\omega C$) vs. real (R) components of the complex impedance, where C is the capacitance of the sample and R its resistance) are shown in Figure S1. At RH below about 60%, only straight lines were observed, indicating very large values of R. At RH larger than 60%, the impedance semicircle started forming, as seen in the inset of Figure S1, which shows values of R obtained from the intercepts of the semicircles with a horizontal axis as a function of humidity for humidity values above 60%. The evolution of R with humidity was similar to that shown by DC measurements, so we decided to use DC for all the following measurements.

Generally, powder pellets were found to be superior both to the single crystals and nanowires in all aspects. While pellets showed logarithmic trends in response over the whole measuring range, single crystals showed a plateau around 50% RH, under which the response did not change (Figure S2). The response of nanowires showed no predictable trend; in fact, a slow degradation of sensing properties was observed over time. In contrast, powder pellets proved to be stable over the one-month period after being stored at ambient conditions: measurements were repeated one month after the initial ones, and an identical value of signal was observed, indicating that no detectable change in the structure nor inclusion of water occurred in that period. Samples began to show the slow diminishment of signal after six months. Between the measurements, the sensor was stored at ambient conditions. The sensor also showed no change in resistivity under CO_2, Ar, N_2 or O_2 exposure, indicating selectivity towards water.

Response and recovery periods are typically measured as the time required for the signal to reach a certain portion of the full value as a response to external stimuli. To be precise, the response time (t_{res}) is the time at which 90% of value $\Delta I_{res} = I_p - I_b$ is reached, starting from the base of the peak, where I_p is the current at the peak of the signal at 55% RH and I_b is the average current at the baseline at 25% RH. By analogy, recovery time (t_{rec}) is the time required for the signal to return to 10% of the mentioned difference. This interval of RH was chosen for responsivity measurements for convenience, since the saturation time of the measuring chamber towards extremely high or low RH would not allow for representative results.

The responsivities of all three types of $MA_3Bi_2Br_9$ sensors were very fast, ranging from 1.5 to 1.7 s, followed by recovery times ranging from 4.1 to 7.1 s obtained from 25 to 55% RH (Figure S3). In comparison, response and recovery times for the commercial Sensirion SHT 31 sensor in the same RH range were t_{res}/t_{rec} = 3.4 s/13.8 s. The best results, again, were obtained for powder pressed in pellets, t_{res}/t_{rec} = 1.5 s/4.1 s.

It became of interest to see whether response/recovery time could be further enhanced by a changing the temperature. A differential thermogravimetric analysis (DTA) experiment showed that $MA_3Bi_2Br_9$ is stable towards thermal decomposition up to >300 °C (Figure S4). Thus, by gentle heating, it was possible to shorten the responsivity times even more, down to t_{res}/t_{rec} = 1.5 s/1.5 s at 35 °C for the 30–65% RH interval (Figure 3). Shorter response and recovery times at higher temperatures were accompanied by a somewhat weaker signal, albeit the signal to noise ratio was still largely within the useful detection range, owing to the high sensitivity of the sample.

To summarize the sensing properties, both the response and recovery times are shorter than for the commercial Sensirion SHT 31 sensor for all three devices (Figure S3). Comparison with several recent literature values is given in Table 1, showing that $MA_3Bi_2Br_9$ sensor is among the fastest ones. While some sensors are reported to have a very fast responses on a tiny RH change (Table 1, entry 6), they experience much longer times when sensing a larger difference in RH. In addition, to prepare faster sensors, typically, thin-film techniques are applied where sensing properties benefit from a smaller amount of absorbing material; however, such an endeavor is beyond the scope of the present study. Rather, a simple, cheap, environmentally friendly device is presented.

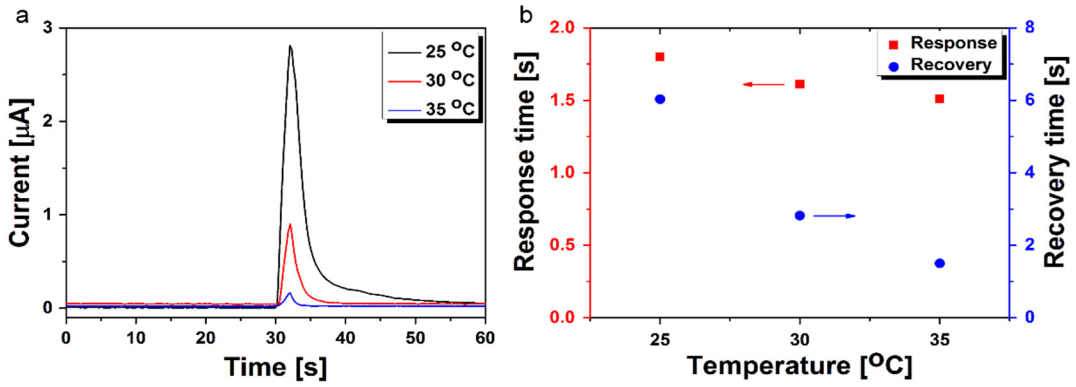

Figure 3. (**a**) Response of $MA_3Bi_2Br_9$ pellets from 30% to 65% RH at several temperatures, (**b**) shortening of response and recovery times with temperature.

Table 1. Comparison of several recent humidity sensors.

No.	Sensor	Operation Range (RH/%)	t_{res}/t_{rec} (Measuring Interval)	Reference
1	PANI	11–97	36/49 s	[50]
2	$CH_3NH_3PbI_{3-x}Cl_x$	30–90	24 s/?	[41]
3	rGO/MoS_2	10–90	17 s/494 s	[51]
4	Graphene oxide	11–97	2.7 s/4.6 s	[52]
5	Nanodiamonds	11–97	0.154 s/0.137 s	[39]
6	Silicon nanocrystals	8–83	0.04 s/0.04 s (20–30% RH) 12 s/2 s (20–95% RH)	[53]
7	$Cs_2BiAgBr_6$	11–75	1.78 s/0.45 s	[42]
8	**Sensirion SHT 31**	**0–100**	**3.4 s/13.8 s (25–55% RH)**	**commercial**
9	$MA_3Bi_2Br_9$ nanowires	1–96	1.7 s/7.1 s (25–55% RH)	Present study
10	$MA_3Bi_2Br_9$ Single crystal	1–96	1.5 s/7.3 s (25–55% RH)	Present study
11	**$MA_3Bi_2Br_9$ pellets, RT**	**1–96**	**1.5 s/4.1 s (25–55% RH)**	**Present study**
12	**$MA_3Bi_2Br_9$ pellets, 35 °C**	**1–96**	**1.5 s/1.5 s (30–65% RH)**	**Present study**

Dynamical measurements of humidity were performed with parallel exposures of two sensors to the short stream of wet air at ambient temperature. Figure 4 shows a comparison of $MA_3Bi_2Br_9$ pellets sensors with the commercial one over several detection cycles; response times were found to be faster than those for the commercial sensor, visible over multiple detection cycles as sharper peaks in the figure. Concerning stability, the same speed was observed in a repeated experiment, performed one month after initial measurements. Noteworthily, all three types of $MA_3Bi_2Br_9$ device produced significantly sharper peaks than the commercial one used as a reference (Figure S3).

From a mechanistic perspective, it seems that the change in the conductivity of the material in contact with a humid atmosphere is confined to surface effects. If I–V measurements are performed on a single crystal sample, a signal remains unchanged until a threshold value of ~50% humidity is reached, after which, it begins to follow a linear trend, similar to the microcrystalline powder sample (Figure S2). The corresponding value of resistance at ~0–50% RH may be attributed to the proper conductivity of material without the contribution of adsorbed water, which effectively masks the detection when measuring resistivity at lower RH.

In contrast, a larger surface of the polycrystalline sample of comparable size allows for more water to be collected into the similar volume of the sensor, resulting in drastically lower resistivity at the same relative humidity; for example, at 50% RH, the resistance of a single crystal is ~10^9 Ω, while in a pressed pellet, it is only ~10^7 Ω. Moreover, in the polycrystalline sample pellets, the grain boundaries increase net resistance at lower RH (with less adsorbed water), allowing for values below the threshold conductivity of the single-crystal material to be measured using I-V measurements (up to ~10^{11} Ω at 0.7%

RH). These observations combined indicate that the conductivity of $MA_3Bi_2Br_9$ is indeed a surface phenomenon.

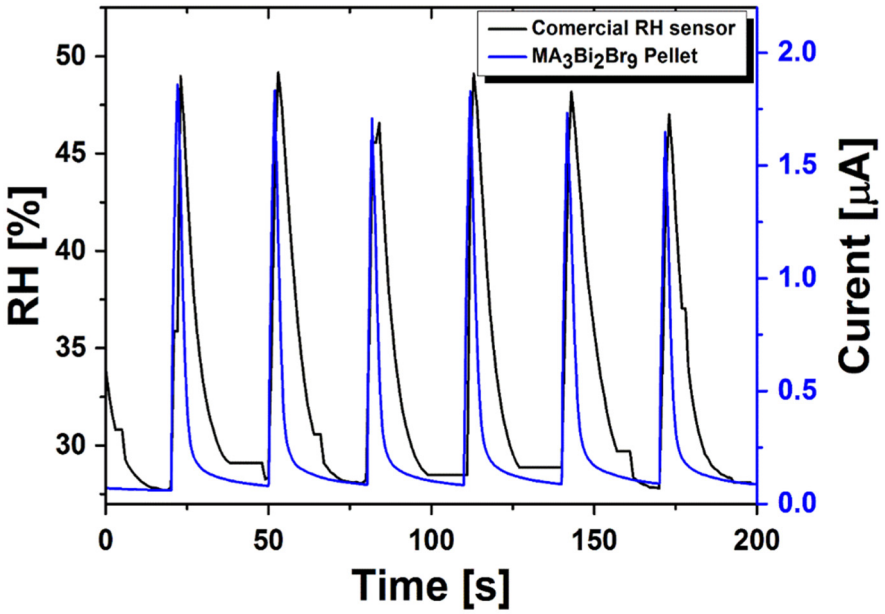

Figure 4. Ambient temperature responsivity of powder pellets over time in comparison to the commercial sensor from RH ~25–50%. The signals were scaled to normal.

This notion is further supported by X-ray measurements of two series of samples sealed in glass ampules: one at 95.7% ("wet") RH and another at 0.3% ("dry") RH. All structure details determined using the single crystal study were confirmed by the Rietveld refinement based on these experiments for both samples. No difference between the "wet" and pristine structures was found. Crystallographic characteristics and the main details of the structure refinement are listed in Table S1 for the "wet" and pristine samples in comparison to the single-crystal data. Figure S5 shows the powder XRD profiles for both of the samples. A slightly higher volume of the unit cell found for the "wet" sample, V_w = 585.36(3) Å^3, in comparison to the pristine one, V_{pr} = 584.88(4) Å^3, can be explained by the amount of absorption water on the surface of crystallites. The presence of water was also confirmed by a slightly higher background characteristic of the XRD profile for the "wet" sample (Figure S5).

Therefore, since no detectable change in X-ray pattern was observed, it may safely be concluded that no water penetrated into the sample structure, as is the case with the well-researched lead derivative, to which structure water is immediately included upon exposure to humidity [41,49]. In $MA_3Bi_2Br_9$, rather, any effect from humidity is confined to the surface of the material, where a conductive effect happens in accordance to the Grotthuss mechanism [54], as suggested by Figure 5.

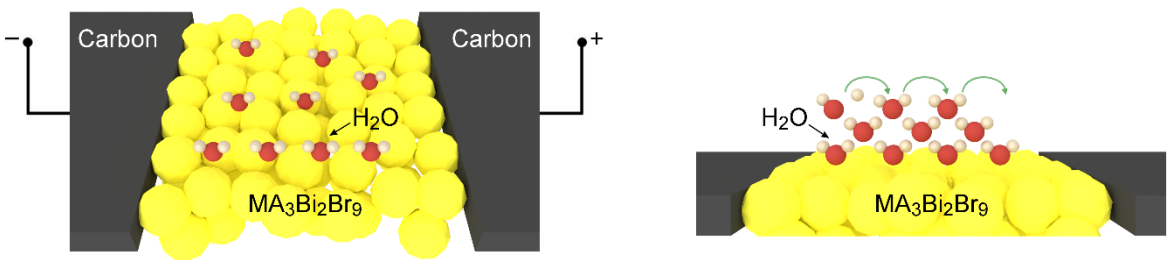

Figure 5. Proposed sensing mechanism. Change in resistivity occurs as a surface phenomenon involving proton hopping between adsorbed molecules.

4. Conclusions

A novel lead-free material for humidity sensors was tested in all of the forms: pellets, single crystals and nanowires. Following the synthesis, a new detailed crystal structural refinement was performed for all the prepared materials, showing that the bulk crystal structure was stable and indifferent to water; rather, the humidity sensing characteristic was due to the surface adsorption.

Sensor properties were measured in both static and dynamic conditions of relative humidity. While the sensor was active over the whole humidity range (0.7–95.8% RH), it was also very fast in comparison to the commercial and literature ones, with response/recovery times of 1.5 s/1.5 s.

Supplementary Materials: The following supporting information can be downloaded at: https://www.mdpi.com/article/10.3390/cryst12040547/s1, Table S1: Experimental details for the $MA_3Bi_2Br_9$ structure determination and refinement; Figure S1. (a) Complex impedance plots (X vs. R) for different humidities. The inset shows formation of the impedance semicircle at relative humidities at and above 60%. (b) AC resistivity R exctracted from data shown in Figure S1a (intercept of Z with R axis at low frequencies); Figure S2. Resistivity of three types of $MA_3Bi_2Br_9$sensor: powder pellets (BP), single crystal (SC) and nanowires (BW). Resistivities are scaled to normal; Figure S3. Comparison of response of three types of $MA_3Bi_2Br_9$ sensor with commercial one; Figure S4. Differential thermogravimetric analysis of $MA_3Bi_2Br_9$; Figure S5. XRD profiles corresponding to the Rietveld refinement of the $MA_3Bi_2Br_9$ structure for the pristine and "wet" samples.

Author Contributions: Conceptualization, V.D., L.F., E.H. and T.I.; Methodology, P.A., A.A., D.D., E.H. and T.I.; Validation, A.A., D.D. and E.H.; Formal Analysis, V.D., P.A., M.K., A.C., A.A., M.V., D.D. and T.I.; Investigation, V.D., P.A., M.K., A.C., A.A. and M.V.; Resources, V.D. and L.F.; Data curation, V.D., P.A., M.K., A.C., A.A., M.V., D.D. and T.I.; Writing—original draft preparation, T.I.; Writing—review and editing, V.D., P.A., A.A., D.D., L.F. and T.I.; Visualization, V.D., P.A., A.C., A.A., D.D. and T.I.; supervision, A.A., D.D., L.F. and T.I.; Project Administration, L.F. and T.I.; Funding acquisition, L.F. All authors have read and agreed to the published version of the manuscript.

Funding: This research was funded by European Research Council grant number 10306 and ERC Advanced grant Picoprop (Project Number: 670918).

Acknowledgments: The authors are grateful for the financial support of the European Research Council (No. 10306). The authors are grateful for the financial support of the ERC Advanced grant Picoprop (Project Number: 670918). We would like to thank BM01 staff for the support and help with the XRD experiments. The allocation of the beamtime at the Swiss–Norwegian Beam Lines (SNBL) by SNX council is greatly appreciated.

Conflicts of Interest: The authors declare no conflict of interest.

References

1. Snaith, H.J. Present Status and Future Prospects of Perovskite Photovoltaics. *Nat. Mater.* **2018**, *17*, 372–376. [CrossRef] [PubMed]
2. Luo, D.; Chen, Q.; Qiu, Y.; Zhang, M.; Liu, B. Device Engineering for All-Inorganic Perovskite Light-Emitting Diodes. *Nanomaterials* **2019**, *9*, 1007. [CrossRef] [PubMed]
3. Ho-Baillie, A. Perovskites Cover Silicon Textures. *Nat. Mater.* **2018**, *17*, 751–752. [CrossRef] [PubMed]
4. Sahli, F.; Werner, J.; Kamino, B.A.; Bräuninger, M.; Monnard, R.; Paviet-Salomon, B.; Barraud, L.; Ding, L.; Leon, J.J.D.; Sacchetto, D.; et al. Fully Textured Monolithic Perovskite/Silicon Tandem Solar Cells with 25.2% Power Conversion Efficiency. *Nat. Mater.* **2018**, *17*, 820–826. [CrossRef] [PubMed]
5. Andričević, P.; Kollár, M.; Mettan, X.; Náfrádi, B.; Sienkiewicz, A.; Fejes, D.; Hernádi, K.; Forró, L.; Horváth, E. Three-Dimensionally Enlarged Photoelectrodes by a Protogenetic Inclusion of Vertically Aligned Carbon Nanotubes into $CH_3NH_3PbBr_3$ Single Crystals. *J. Phys. Chem. C* **2017**, *121*, 13549–13556. [CrossRef]
6. Spina, M.; Lehmann, M.; Náfrádi, B.; Bernard, L.; Bonvin, E.; Gaál, R.; Magrez, A.; Forró, L.; Horváth, E. Microengineered $CH_3NH_3PbI_3$ Nanowire/Graphene Phototransistor for Low-Intensity Light Detection at Room Temperature. *Small* **2015**, *11*, 4824–4828. [CrossRef]
7. Andričević, P.; Mettan, X.; Kollár, M.; Náfrádi, B.; Sienkiewicz, A.; Garma, T.; Rossi, L.; Forró, L.; Horváth, E. Light-Emitting Electrochemical Cells of Single Crystal Hybrid Halide Perovskite with Vertically Aligned Carbon Nanotubes Contacts. *ACS Photonics* **2019**, *6*, 967–975. [CrossRef]

8. Lin, K.; Xing, J.; Quan, L.N.; de Arquer, F.P.G.; Gong, X.; Lu, J.; Xie, L.; Zhao, W.; Zhang, D.; Yan, C.; et al. Perovskite Light-Emitting Diodes with External Quantum Efficiency Exceeding 20 per Cent. *Nature* **2018**, *562*, 245. [CrossRef]
9. Liu, B.; Wang, L.; Gu, H.; Sun, H.; Demir, H.V. Highly Efficient Green Light-Emitting Diodes from All-Inorganic Perovskite Nanocrystals Enabled by a New Electron Transport Layer. *Adv. Opt. Mater.* **2018**, *6*, 1800220. [CrossRef]
10. Zhao, X.; Xu, H.; Wang, Z.; Lin, Y.; Liu, Y. Memristors with Organic-Inorganic Halide Perovskites. *InfoMat* **2019**, *1*, 183–210. [CrossRef]
11. Mettan, X.; Pisoni, R.; Matus, P.; Pisoni, A.; Jaćimović, J.; Náfrádi, B.; Spina, M.; Pavuna, D.; Forró, L.; Horváth, E. Tuning of the Thermoelectric Figure of Merit of $CH_3NH_3MI_3$ (M=Pb,Sn) Photovoltaic Perovskites. *J. Phys. Chem. C* **2015**, *119*, 11506–11510. [CrossRef]
12. Náfrádi, B.; Szirmai, P.; Spina, M.; Lee, H.; Yazyev, O.V.; Arakcheeva, A.; Chernyshov, D.; Gibert, M.; Forró, L.; Horváth, E. Optically Switched Magnetism in Photovoltaic Perovskite CH_3NH_3(Mn:Pb)I_3. *Nat. Commun.* **2016**, *7*, 13406. [CrossRef] [PubMed]
13. Benmessaoud, I.R.; Mahul-Mellier, A.-L.; Horváth, E.; Maco, B.; Spina, M.; Lashuel, H.A.; Forró, L. Health Hazards of Methylammonium Lead Iodide Based Perovskites: Cytotoxicity Studies. *Toxicol. Res.* **2016**, *5*, 407–419. [CrossRef] [PubMed]
14. Babayigit, A.; Ethirajan, A.; Muller, M.; Conings, B. Toxicity of Organometal Halide Perovskite Solar Cells. *Nat. Mater.* **2016**, *15*, 247–251. [CrossRef]
15. DuPont, H.L. Travelers' Diarrhea: Antimicrobial Therapy and Chemoprevention. *Nat. Clin. Pract. Gastroenterol. Hepatol.* **2005**, *2*, 191. [CrossRef]
16. Attique, S.; Ali, N.; Ali, S.; Khatoon, R.; Li, N.; Khesro, A.; Rauf, S.; Yang, S.; Wu, H. A Potential Checkmate to Lead: Bismuth in Organometal Halide Perovskites, Structure, Properties, and Applications. *Adv. Sci.* **2020**, *7*, 1903143. [CrossRef]
17. Abulikemu, M.; Ould-Chikh, S.; Miao, X.; Alarousu, E.; Murali, B.; Ndjawa, G.O.N.; Barbé, J.; Labban, A.E.; Amassian, A.; Gobbo, S.D. Optoelectronic and Photovoltaic Properties of the Air-Stable Organohalide Semiconductor $(CH_3NH_3)_3Bi_2I_9$. *J. Mater. Chem. A* **2016**, *4*, 12504–12515. [CrossRef]
18. Jakubas, R.; Krzewska, U.; Bator, G.; Sobczyk, L. Structure and Phase Transition in $(CH_3NH_3)_3Bi_2Br_9$. A Novel Improper Ferroelectrics. *Ferroelectrics* **1988**, *77*, 129–135. [CrossRef]
19. Matuszewski, J.; Jakubas, R.; Sobczyk, L.; Głowiak, T. Structure of Pentakis(Methylammonium) Undecabromodibismuthate. *Acta Crystallogr. Sect. C Cryst. Struct. Commun.* **1990**, *46*, 1385–1388. [CrossRef]
20. Jakubas, R. A New Ferroelectric Compound: $(CH_3NH_3)_5Bi_2Br_{11}$. *Solid State Commun.* **1989**, *69*, 267–269. [CrossRef]
21. Ishihara, H.; Watanabe, K.; Iwata, A.; Yamada, K.; Kinoshita, Y.; Okuda, T.; Krishnan, V.G.; Dou, S.; Weiss, A. NQR and X-Ray Studies of $[N(CH_3)_4]_3M_2X_9$ and $(CH_3NH_3)_3M_2X_9$ (M = Sb,Bi; X = Cl,Br). *Z. Nat. A* **1992**, *47*, 65–74. [CrossRef]
22. Bator, G. AC and DC Conductivity around the Ferroelectric Phase Transition in $(CH_3NH_3)_3Bi_2Br_9$ (MABB) Crystal. *Ferroelectrics* **1997**, *200*, 287–295. [CrossRef]
23. Jakubas, R.; Bator, G.; Mróz, J. Dielectric and Pyroelectric Properties of $(CH_3NH_3)_3Bi_2Br_9$ Crystals in the Ferroelectric Phase Transition Region. *Ferroelectrics* **1993**, *146*, 65–71. [CrossRef]
24. Wojtaś, M.; Reece, M.J. Dynamics of Ferroelectric Switching of $[H_3CNH_3]_5[Bi_2Br_{11}]$. *J. Appl. Phys.* **2012**, *111*, 024108. [CrossRef]
25. Hoye, R.L.Z.; Brandt, R.E.; Osherov, A.; Stevanović, V.; Stranks, S.D.; Wilson, M.W.B.; Kim, H.; Akey, A.J.; Perkins, J.D.; Kurchin, R.C.; et al. Methylammonium Bismuth Iodide as a Lead-Free, Stable Hybrid Organic-Inorganic Solar Absorber. *Chem. A Eur. J.* **2016**, *22*, 2605–2610. [CrossRef]
26. Park, B.-W.; Philippe, B.; Zhang, X.; Rensmo, H.; Boschloo, G.; Johansson, E.M.J. Bismuth Based Hybrid Perovskites $A_3Bi_2I_9$ (A: Methylammonium or Cesium) for Solar Cell Application. *Adv. Mater.* **2015**, *27*, 6806–6813. [CrossRef]
27. Farahani, H.; Wagiran, R.; Hamidon, M.N. Humidity Sensors Principle, Mechanism, and Fabrication Technologies: A Comprehensive Review. *Sensors* **2014**, *14*, 7881–7939. [CrossRef]
28. Khan, Y.; Ostfeld, A.E.; Lochner, C.M.; Pierre, A.; Arias, A.C. Monitoring of Vital Signs with Flexible and Wearable Medical Devices. *Adv. Mater.* **2016**, *28*, 4373–4395. [CrossRef]
29. Folke, M.; Cernerud, L.; Ekström, M.; Hök, B. Critical Review of Non-Invasive Respiratory Monitoring in Medical Care. *Med. Biol. Eng. Comput.* **2003**, *41*, 377–383. [CrossRef]
30. Lou, Z.; Wang, L.; Shen, G. Recent Advances in Smart Wearable Sensing Systems. *Adv. Mater. Technol.* **2018**, *3*, 1800444. [CrossRef]
31. Zou, Z.; Zhu, C.; Li, Y.; Lei, X.; Zhang, W.; Xiao, J. Rehealable, Fully Recyclable, and Malleable Electronic Skin Enabled by Dynamic Covalent Thermoset Nanocomposite. *Sci. Adv.* **2018**, *4*, eaaq0508. [CrossRef] [PubMed]
32. Horváth, E.; Ribič, P.R.; Hashemi, F.; Forró, L.; Magrez, A. Dye Metachromasy on Titanate Nanowires: Sensing Humidity with Reversible Molecular Dimerization. *J. Mater. Chem.* **2012**, *22*, 8778. [CrossRef]
33. Chen, M.; Xue, S.; Liu, L.; Li, Z.; Wang, H.; Tan, C.; Yang, J.; Hu, X.; Jiang, X.-F.; Cheng, Y.; et al. A Highly Stable Optical Humidity Sensor. *Sens. Actuators B Chem.* **2019**, *287*, 329–337. [CrossRef]
34. Xu, W.; Li, F.; Cai, Z.; Wang, Y.; Luo, F.; Chen, X. An Ultrasensitive and Reversible Fluorescence Sensor of Humidity Using Perovskite $CH_3NH_3PbBr_3$. *J. Mater. Chem. C* **2016**, *4*, 9651–9655. [CrossRef]
35. Domenegueti, J.F.M.; Zilio, S.C. Humidity and Pressure Sensor Based on Internal Reflection. *Appl. Opt.* **2014**, *53*, 1591–1596. [CrossRef]
36. Tian, Q.; Yang, H.; Rong, Q.; Feng, Z.; Wang, R.; Zaini, M.K.A.B.; Lim, K.-S.; Ahmad, H.; Zhang, P.; Ding, X.; et al. Highly Sensitive Micro-Hygrometer Based on Microfiber Knot Resonator. *Opt. Commun.* **2019**, *431*, 88–92. [CrossRef]

37. Muhammad, F.; Tahir, M.; Zeb, M.; Wahab, F.; Kalasad, M.N.; Khan, D.N.; Karimov, K.S. Cadmium Selenide Quantum Dots: Synthesis, Characterization and Their Humidity and Temperature Sensing Properties with Poly-(Dioctylfluorene). *Sens. Actuators B Chem.* **2019**, *285*, 504–512. [CrossRef]
38. Zheng, Z.; Yao, Y.; Sun, Y.; Yeow, J.T.W. Development of a Highly Sensitive Humidity Sensor Based on the Capacitive Micromachined Ultrasonic Transducer. *Sens. Actuators B Chem.* **2019**, *286*, 39–45. [CrossRef]
39. Yu, X.; Chen, X.; Yu, X.; Chen, X.; Ding, X.; Zhao, X. Flexible Wearable Humidity Sensor Based on Nanodiamond with Fast Response. *IEEE Trans. Electron Devices* **2019**, *66*, 1911–1916. [CrossRef]
40. Zhu, Z.; Sun, Q.; Zhang, Z.; Dai, J.; Xing, G.; Li, S.; Huang, X.; Huang, W. Metal Halide Perovskites: Stability and Sensing-Ability. *J. Mater. Chem. C* **2018**, *6*, 10121–10137. [CrossRef]
41. Ren, K.; Huang, L.; Yue, S.; Lu, S.; Liu, K.; Azam, M.; Wang, Z.; Wei, Z.; Qu, S.; Wang, Z. Turning a Disadvantage into an Advantage: Synthesizing High-Quality Organometallic Halide Perovskite Nanosheet Arrays for Humidity Sensors. *J. Mater. Chem. C* **2017**, *5*, 2504–2508. [CrossRef]
42. Weng, Z.; Qin, J.; Umar, A.A.; Wang, J.; Zhang, X.; Wang, H.; Cui, X.; Li, X.; Zheng, L.; Zhan, Y. Lead-Free $Cs_2BiAgBr_6$ Double Perovskite-Based Humidity Sensor with Superfast Recovery Time. *Adv. Funct. Mater.* **2019**, *29*, 1902234. [CrossRef]
43. Kollár, M.; Ćirić, L.; Dil, J.H.; Weber, A.; Muff, S.; Ronnow, H.M.; Náfrádi, B.; Monnier, B.P.; Luterbacher, J.S.; Forró, L.; et al. Clean, Cleaved Surfaces of the Photovoltaic Perovskite. *Sci. Rep.* **2017**, *7*, 695. [CrossRef] [PubMed]
44. Dyadkin, V.; Pattison, P.; Dmitriev, V.; Chernyshov, D. A New Multipurpose Diffractometer PILATUS@SNBL. *J. Synchrotron. Rad.* **2016**, *23*, 825–829. [CrossRef]
45. Oxford Diffraction. *CrysAlisPRO*; Version 1.171.37.35; Agilent Technologies: Santa Clara, CA, USA, 2014.
46. Petříček, V.; Dušek, M.; Palatinus, L. Crystallographic Computing System JANA2006: General Features. *Z. Krist. Cryst. Mater.* **2014**, *229*, 345–352. [CrossRef]
47. Palatinus, L.; Chapuis, G. SUPERFLIP—a Computer Program for the Solution of Crystal Structures by Charge Flipping in Arbitrary Dimensions. *J. Appl. Cryst.* **2007**, *40*, 786–790. [CrossRef]
48. Lazarini, F. Caesium Enneabromodibismuthate(III). *Acta Cryst. B* **1977**, *33*, 2961–2964. [CrossRef]
49. Arakcheeva, A.; Chernyshov, D.; Spina, M.; Forró, L.; Horváth, E. $CH_3NH_3PbI_3$: Precise Structural Consequences of Water Absorption at Ambient Conditions. *Acta Cryst. B* **2016**, *72*, 716–722. [CrossRef]
50. Manjunatha, S.; Machappa, T.; Ravikiran, Y.T.; Chethan, B.; Sunilkumar, A. Polyaniline Based Stable Humidity Sensor Operable at Room Temperature. *Phys. B Condens. Matter* **2019**, *561*, 170–178. [CrossRef]
51. Park, S.Y.; Lee, J.E.; Kim, Y.H.; Kim, J.J.; Shim, Y.-S.; Kim, S.Y.; Lee, M.H.; Jang, H.W. Room Temperature Humidity Sensors Based on RGO/MoS2 Hybrid Composites Synthesized by Hydrothermal Method. *Sens. Actuators B Chem.* **2018**, *258*, 775–782. [CrossRef]
52. He, P.; Brent, J.R.; Ding, H.; Yang, J.; Lewis, D.J.; O'Brien, P.; Derby, B. Fully Printed High Performance Humidity Sensors Based on Two-Dimensional Materials. *Nanoscale* **2018**, *10*, 5599–5606. [CrossRef] [PubMed]
53. Kano, S.; Kim, K.; Fujii, M. Fast-Response and Flexible Nanocrystal-Based Humidity Sensor for Monitoring Human Respiration and Water Evaporation on Skin. *ACS Sens.* **2017**, *2*, 828–833. [CrossRef] [PubMed]
54. Agmon, N. The Grotthuss Mechanism. *Chem. Phys. Lett.* **1995**, *244*, 456–462. [CrossRef]